RSC Advances

PAPER

View Article Online
View Journal | View Issue



Cite this: *RSC Adv.*, 2021, **11**, 3695

# Degradation of ammonia gas by $Cu_2O$/{001}$TiO_2$ and its mechanistic analysis

Jiaming Zhu,[ab] Yue Jian,[ab] Dingbiao Long,[ab] Hao Wang,[ab] Yaqiong Zeng,[ab] Jigang Li,[a] Rong Xiao*[a] and Shihua Pu*[ab]

A heterogeneous composite catalyst $Cu_2O$/{001}$TiO_2$ was successfully prepared by the impregnation–reduction method. With ammonia as the target pollutant, the degradation performance and degradation mechanism analysis of the prepared composite catalyst were investigated, providing technology for the application of photocatalysis technology in ammonia treatment reference. The catalysts were characterized by X-ray diffraction (XRD), transmission electron microscopy (TEM), X-ray photoelectron spectroscopy (XPS), scanning electron microscopy (SEM), specific surface area (BET), fluorescence spectrum (PL) and UV-visible absorption (UV-Vis). The results showed: compared with single {001}$TiO_2$, the addition of $Cu_2O$ to form a composite catalyst can reduce the recombination of electron–hole pairs, resulting in increased absorption intensity in the visible light range, decreased band gap width, and finally improved the degradation performance. When the composite ratio is 1 : 10, the specific surface area is the largest, which is 72.51 $m^2$ $g^{-1}$, and the degradation rate of ammonia is also the highest maintained at 85%. After repeated use for 5 times, the degradation rate of ammonia decreases gradually due to the loss of catalyst and photo-corrosion. In the whole reaction process, surface adsorbed water and associated hydroxyl radical participate in the ammonia degradation reaction, and finally form free hydroxyl radical and $NO_3^-$. It provides some theoretical support for ammonia gas treatment, which is of great significance to protect the environment.

Received 11th December 2020
Accepted 11th January 2021

DOI: 10.1039/d0ra10431k

rsc.li/rsc-advances



## 1. Introduction

Atmospheric ammonia is the sole abundant alkaline gas and contributes substantially to the formation of particulate matter, which affects air quality and has implications for human health and life expectancy.[1,2] China emits about 10–15 million tons $NH_3$ to the air each year, almost doubled the sum in the USA and European Union.[3] At present, nitrogen deposition per square kilometer of Beijing–Tianjin–Hebei region in China reaches 6.1 tons per year, which is the highest level recorded in developed countries.[4] The ammonia from animal husbandry may not only cause global climate change, but can also bring disease in animals and humans, such as paralysis centralis, endobronchitis, and others.[5] Reducing $NH_3$ emission can significantly improve China's air quality, especially in North China Plain where haze pollution is severe in winter.[6]

According to 2016 Clean Air Management Report from CAAC (Clean Air Alliance of China), 80% of China ammonia emissions comes from intensive livestock farm and fertilizer application. Therefore the Chinese central government has started to put agricultural $NH_3$ on the reduction list for air quality in the updated Clean Air Act (CAA) given its important contribution to PM2.5 pollution,[7] but it is important that solutions are mainly constrained by the implementation of effective technologies in agricultural industry. In the past, livestock farms adopted traditional physical methods of adsorption and ventilation to eliminate the ammonia generated. Although they can decrease the release concentration of ammonia over time, but cannot reduce the total amount of ammonia emissions. The traditional process of ammonia treatment has high cost and short of stability, may aggravate the secondary pollution of the environment.[8]

Photocatalysis technology is more and more popular due to its low reaction temperature and no secondary pollution in the reaction process. The main principle of photocatalysis technology is based on the oxidation–reduction ability of photocatalyst under light conditions, so as to achieve purification of pollution.[9] It has good application effects in many frontier fields such as sewage treatment,[10] waste gas treatment,[11] energy development,[12] self-cleaning material[13] and antibacterial[14] and other fields.

$TiO_2$ has become the most promising photocatalyst due to its advantages such as good chemical stability, safety, non-toxicity, and strong redox ability.[15] However, due to the wide band gap width (3.2 eV) of $TiO_2$, it can only respond to ultraviolet light

[a]*Chongqing Academy of Animal Sciences, Chongqing, 402460, China. E-mail: XRD610@126.com; x00r@163.com; pu88962@126.com*

[b]*Scientific Observation and Experiment Station of Livestock Equipment Engineering in Southwest, Ministry of Agriculture, Chongqing, 402460, China*

with high energy, while the ultraviolet content in the solar spectrum is very low, resulting in its low utilization rate. At the same time, the photoelectron–hole composite rate of $TiO_2$ is high, which reduces its activity and seriously hinders its practical application.[16] In the photocatalytic reaction system, the activity of $TiO_2$ is related to crystal shape, morphology and size, *etc.* Recent literatures have shown that crystal surface is also one of the factors affecting its catalytic activity, because the reaction is mainly on the surface of $TiO_2$, the different crystal surfaces has different electron composition and energy band. The anatase $TiO_2$ average surface energy on {001} surface (0.90 J $m^{-2}$) is much higher than that on {101} surface (0.44 J $m^{-2}$).[17] So the crystal growth process is mainly along {101} faces with low surface energy, anatase $TiO_2$ is mainly composed of {101} crystal faces.[18] H. Park *et al.* found that fluoride ion can not only exchange hydroxyl on the $TiO_2$ surface, but also reduce the surface energy of {001} crystal faces.[19] Then, Yang *et al.* synthesized 47% {001} crystal surface $TiO_2$ with HF, of which the activity was much higher than that of {101} crystal surface.[20] Since then, {001}$TiO_2$ has been widely used in environmental governance, sensors, energy development and other fields.[21] Among many semiconductors, $Cu_2O$ has simple preparation process, low raw material price, environmental-friendly and a good response in the visible light range, it is a green catalyst with great development prospect.[22] As a p-type semiconductor, it can be coupled with n-type semiconductor {001}$TiO_2$ to form a heterostructure, and exhibit better performance than a single material. That make it currently widely used in hydrogen production, solar cells, degrade pollutants.[23]

UV lamps are mostly used in the photocatalytic degradation of ammonia. In this paper, a $Cu_2O$/{001}$TiO_2$ composite photocatalyst was prepared and degraded ammonia with xenon lamp. The activity and degradation mechanism of the prepared catalysts for active catalytic degradation of ammonia were investigated, the photocatalytic degradation of ammonia and the composite mechanism of semiconductor were also studied, which provides a certain theoretical basis for improving air quality.

## 2. Experimental

### 2.1 Chemicals

Butyl titanate (AR, Tianjin Fuchen Chemical Reagent Factory), anhydrous ethanol (AR, Tianjin Fuyu Fine Chemical Co., Ltd.), hydrofluoric acid (AR, Sichuan Xilong Chemical Co., Ltd.), sodium hydroxide (AR, Chengdu Kelong Chemical Reagent Factory), anhydrous copper sulfate (AR, Chengdu Cologne Chemical Co., Ltd.), glucose (AR, Chengdu Cologne Chemical Co., Ltd.), P25 (Degussa).

### 2.2 Synthesis of the samples

Anhydrous ethanol (30.4 mL) was slowly added to 35.2 mL butyl titanate and stirred until the solution was well distributed (designated solution A). Then, 30.4 mL absolute ethanol was slowly added to 180 mL ultra-pure water; 12 mL hydrofluoric acid was then added to this solution (designated solution B).

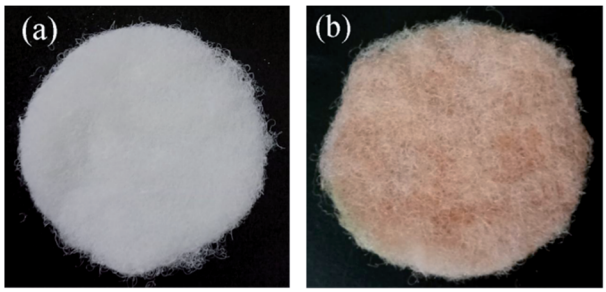


Fig. 1 The loading condition (a) the blank carrier, (b) the loaded carrier with 1 : 10 catalyst.

Next, the A solution was added to the B solution and was stirred under medium speed at room temperature for 2 h; the $TiO_2$ gel was allowed to sit for 2 days and then moved to a stainless-steel reactor containing a Poly Tetra Fluoro Ethylene (PTFE) inner container at 100 °C for 2 h. After cooling, the precipitates were separated and washed alternately with ultra-pure water and absolute ethanol for three times, drying in a 100 °C drying oven. After completion of a grinding process, the obtained powder was marked as {001}$TiO_2$.

8 g anhydrous copper sulfate was dissolved in 100 mL ultrapure water formed as solution A. 6.4 g of sodium hydroxide was dissolved in 20 mL ultrapure water formed as solution B. 12 g glucose was dissolved in 75 mL ultrapure water, which placed the glucose solution at a constant temperature of 34 °C formed as solution C. The solution B added into the solution A form a blue precipitate, which was dropwise added the heated glucose solution; then heated to 70 °C and kept for 15 minutes, and finally appeared a brick red precipitate. Taken a certain amount of brick red precipitate to 100 mL distilled water as well as added 2 g of {001}$TiO_2$, then putted in ultrasonic cleaning machine for 20 min to make it dispersion uniform as mixed solution. After centrifuged the mixed solution, taken the precipitate washed with absolute ethanol and ultrapure water alternatively, which dried and grinded in a blast drying oven at 60 °C to obtain composite catalysts in different proportions, denoted as $Cu_2O$/{001}$TiO_2$ 1 : $X$ (as 1 : 1, 1 : 5, 1 : 10, 1 : 15). The prepared catalyst showed in Fig. 1. The prepared catalyst changes from dark brick red to light brick red with the proportion of {001}$TiO_2$ increases.

We used polyester fiber with good light permeability as the catalyst carrier, the cutted PET carrier into the catalyst gel after repeated washing as the loaded carrier, and the cutted PET carrier into ultrapure water as the blank carrier. Then shook the in the room temperature oscillator for 4 h, then dried in 60 °C air drying oven, as shown in Fig. 1.

### 2.3 Characterization

The X-ray diffractometer (XRD, Germany, Bruker) model D8 Advance was used to test the characteristics of the catalyst crystals at 40 mA and 30 kV, the scanning range was 10–80°, the operating parameters were X-ray tube target = Cu. The transmission electron microscope (TEM, USA, Tecnai G2 F20) was used to test the detailed lattice spacing. Elemental and valence

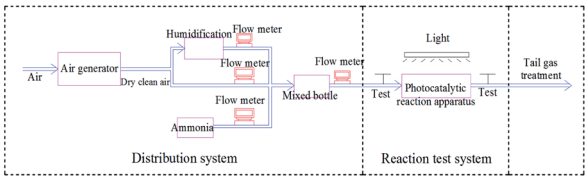


Fig. 2 Schematic diagram of photocatalytic ammonia degradation device.

analysis was carried out using An X-ray photoelectron spectroscopy (XPS, USA, Thermo) model EscaLab 250Xi, the binding energy of the surface adsorbing carbon, C 1s (284.6 eV), was used as the internal standard for calibration. The scanning electron microscope (SEM, Japan, JEOL) model JSM-6700 was used to observe the morphology and dispersion of the samples, the operating voltage was 5.0 kV and the magnification was between 1 and 200 000 times. The TriStar II 3020 series automatic specific surface analyzer (BET, USA, GA) was used to determine the specific surface area and porosity of the catalysts, the catalyst was pretreated at 200 °C and vacuum degassed for 5 hours, and high-purity nitrogen was adsorbed at 77 K. The fluorescence spectrophotometer (PL, Hitachi, Japan) model F-2700 was used to measure the electron–hole recombination, the operating voltage was 250 V, the wavelength was 5 nm, and the excitation wavelength was 300 nm.

### 2.4 Photocatalytic activity measurement

The pipeline after the photocatalytic reaction tube was equipped with a branch pipe as the sample gas outlet, as shown in Fig. 2, using the PGM-7800 ammonia detector manufactured by REA, the two ends of the gas inlet and the gas outlet were tested at an interval of 20 minutes. A 300 W xenon light was used to simulate sunlight for photocatalytic reaction, and the catalytic performance of the catalysts were analyzed and evaluated by measuring the ammonia concentration at the inlet and outlet of the photocatalytic reaction tube.

### 2.5 Degradation of ammonia by different samples

Carriers of blank group, P25, $Cu_2O$, {001}$TiO_2$, 1 : 1, 1 : 5, 1 : 10 and 1 : 15 were put into the reaction tube, the air flow rate was 0.5 L $min^{-1}$, the humidity was 75%, and the photocatalytic reaction was carried out after the gas supply system was stable, we conducted three times and calculated the average value for each set of degradation experiments.

### 2.6 The sample stability

Take 1 : 10 sample and put them into the photocatalytic reaction tube respectively to ensure that the amount of the final supported catalyst is 500 mg. The initial concentration of ammonia is 120 ppm, the humidity is 75%, and the air flow is 0.5 L $min^{-1}$. After the gas supply system is stabilized, the light source used a 300 W long arc xenon lamp to simulate sunlight for the photocatalytic reaction. After the completion of the first photocatalytic degradation, the carrier was taken out and placed in air drying oven at 60 °C for 30 min. The purpose was to remove residual ammonia molecules on the surface, and then the second photocatalytic degradation reaction was conducted, which was repeated for 5 times under the same conditions.

### 2.7 Ammonia degradation mechanism analysis

The method of photocatalytic ammonia was explored by measuring Fourier transform infrared spectroscopy (FT-IR) at different reaction time points. 1 g of 1 : 10 composite catalyst was paved into the sample tank of the static ammonia degradation device, and 500 ppm high concentration ammonia was introduced into the reaction tube. The high concentration of ammonia was conducive to the enrichment of the products on the surface of the catalyst, under xenon light irradiation, samples were taken at 10, 20 and 30 min of the reaction respectively, and Fourier transform infrared spectroscopy (FT-IR) was used to observe the group changes in the reaction process.

## 3. Results and discussion

### 3.1 XRD analysis

It can be seen from Fig. 3 that the characteristic peaks of the prepared {001} $TiO_2$ catalyst at $2\theta$ = 25.28°, 37.80°, 48.04°, 53.89°, 55.06°, 62.68°, 70.31° and 75.03°, respectively correspond to {101}, {004}, {200}, {105}, {211}, {204}, {220} and {215} planes, which are almost identical with anatase $TiO_2$ (JCPDS no. 21-1272).[24] The characteristic peaks of $Cu_2O$ at $2\theta$ = 29.63°, 36.50°, 42.40°, 52.58°, 63.52°, 73.70° and 77.57° correspond to {110}, {111}, {200}, {211}, {220}, {311}, {222}, respectively, almost in accordance with the standard card of $Cu_2O$ (JCPDS no. 65-3288),[25] and there are no peaks of CuO and Cu, indicating that the prepared catalyst is $Cu_2O$ with high purity.

It can be seen that the main characteristic peak of 1 : 1 was basically consistent with the diffraction peak of $Cu_2O$, and the

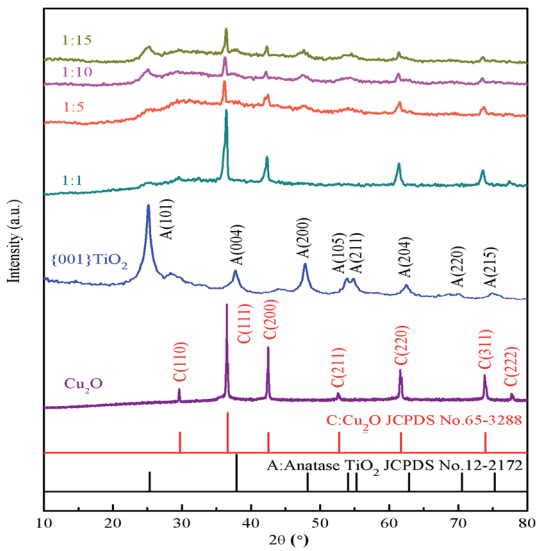


Fig. 3 XRD diagram of samples.

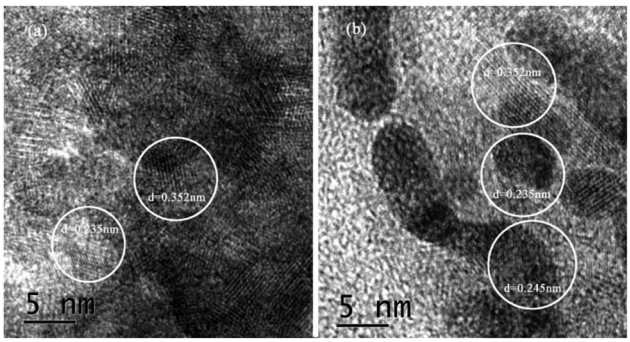


Fig. 4 TEM images of samples (a) {001}$TiO_2$, (b) 1 : 10.

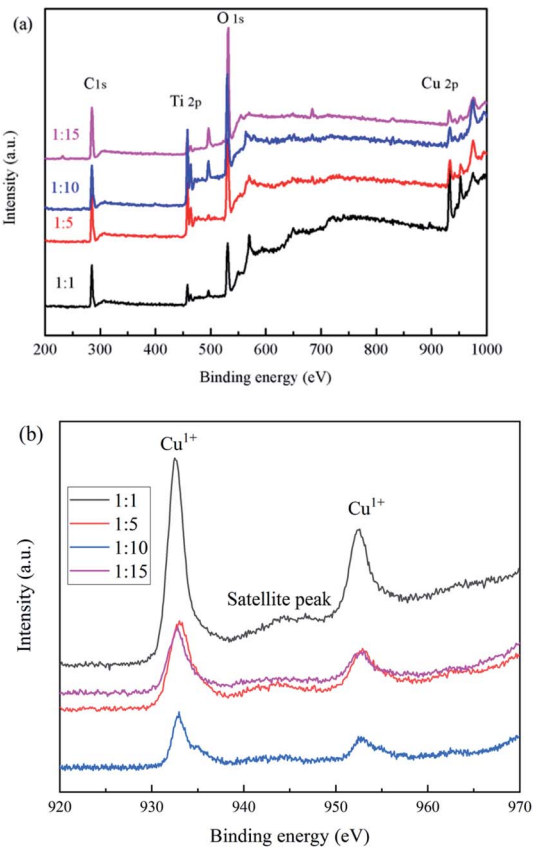


Fig. 5 XPS spectra of the samples (a) full spectrum, (b) Cu 2p.

content of $TiO_2$ was too small to observe. As the composite ratio increases (from 1 : 5 to 1 : 15), the main characteristic peaks of $TiO_2$ appeared gradually at $2\theta = 25.28°$ and 48.04°, and the intensity gradually increased. The characteristic peak of both $TiO_2$ and $Cu_2O$ can still be observed, this means that $TiO_2$ in the prepared composite catalyst has high activity of {001} crystal surface.

### 3.2 TEM analysis

Fig. 4 showed the lattice spacing of {001}$TiO_2$ and 1 : 10, respectively. Fig. 4(a) showed that $d = 0.352$ nm and $d = 0.235$ nm, which correspond to the {101} and {001} planes of anatase $TiO_2$, respectively;[26] Fig. 4(b) not only contains $d = 0.352$ nm and $d = 0.235$ nm, but also contain $d = 0.245$ nm, corresponding to the {111} surface of $Cu_2O$,[27] which meaned that 1 : 10 also contains {001} highly active surface, which is consistent with the XRD analysis results.

### 3.3 XPS analysis

The elemental and valence states of the composite catalysts were analyzed by XPS in Fig. 5. It can be seen that Fig. 5(a) showed that the full spectrum of the catalysts, all catalysts contain C 1s, Ti 2p, O 1s, F 1s, Cu 2p; Fig. 5(b) showed the binding energy of Cu 2p, we found that the prepared catalysts all have characteristic peaks near 932.9 and 952.6 eV, which correspond to $Cu^{1+}$,[28] and the satellite peak was attributed to the shakeup of outer electron in CuO, which indicates only a little CuO in composite samples.[29]

### 3.4 SEM analysis

It can be seen from Fig. 6(a) that the prepared {001}$TiO_2$ was extruded spherical with slightly agglomeration phenomenon. Fig. 6(b) can see that the prepared $Cu_2O$ was in pyramid shape. Fig. 6(c) can see that when the amount of {001}$TiO_2$ was low, it embedded on the surface of $Cu_2O$. Fig. 6(d) can see the {001}

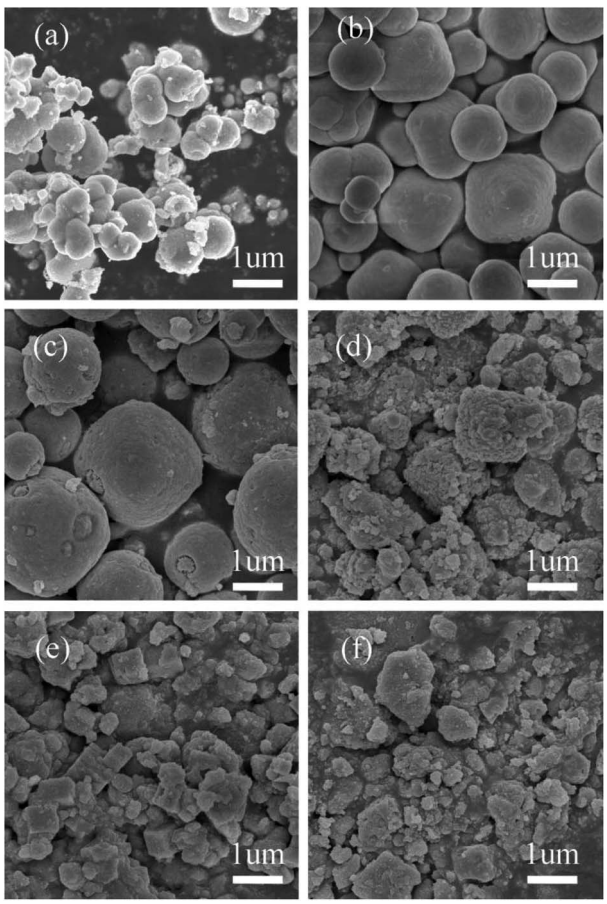


Fig. 6 SEM image of the samples (a) {001}$TiO_2$, (b) $Cu_2O$, (c) 1 : 1, (d) 1 : 5, (e) 1 : 10, (f) 1 : 15.

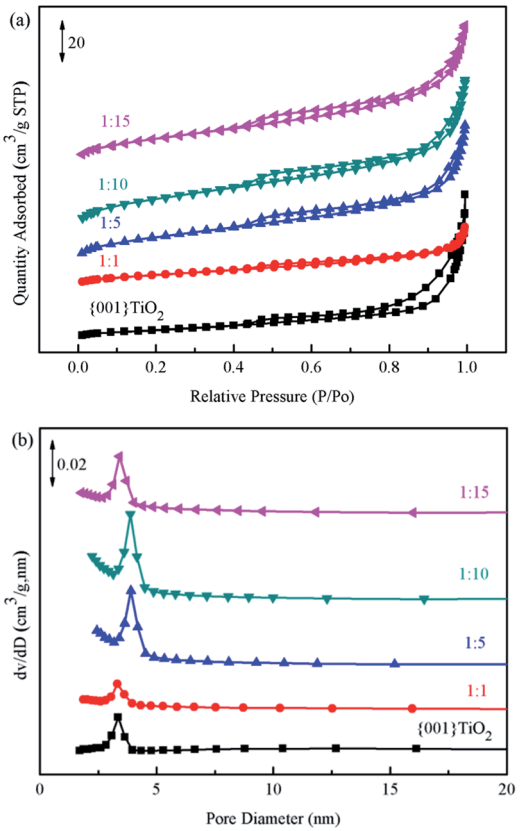


Fig. 7 BET spectrum of the samples (a) specific surface area of catalyst, (b) distribution of catalyst pores.

Table 1 Catalysts information

| Samples | Specific surface area ($m^2$ $g^{-1}$) | Pore volume ($cm^3$ $g^{-1}$) |
|---|---|---|
| {001}$TiO_2$ | 22.79 | 0.09 |
| 1 : 1 | 47.65 | 0.04 |
| 1 : 5 | 58.19 | 0.10 |
| 1 : 10 | 72.51 | 0.11 |
| 1 : 15 | 53.29 | 0.10 |

$TiO_2$ densed growth on $Cu_2O$ surface when the $Cu_2O$/{001}$TiO_2$ is 1 : 5, Fig. 6(e) can be seen there was no regular shape that the particles of each other are stacked together to form a relatively rich pore structure with the $Cu_2O$/{001}$TiO_2$ is 1 : 10. Fig. 6(f) showed the various particles pile up each other appeared obvious agglomeration when the $Cu_2O$/{001}$TiO_2$ is 1 : 15, that may be due to when the amount of {001}$TiO_2$ was excessive, it will be formed a large number of fragments after ultrasonic dispersion and energy absorption, and appeared the agglomeration in the recombination process of the composite.

### 3.5 BET analysis

Brunauer–Emmett–Teller (BET) method was used to calculate the specific surface area of the prepared catalyst, and Barrett–Joyner–Halenda (BJH) method was used to analyze the pore size distribution and pore volume.[31] The catalysts in Fig. 7(a) showed typical type IV nitrogen adsorption desorption isotherms. The pore size distribution of the catalysts in Fig. 7(b) showed that the pore size of the prepared catalyst was mainly concentrated in 0–20 nm, indicating that the pore size of the catalyst was mainly mesoporous. Combined with the data in Table 1, the specific surface area of 1 : 10 was the largest, which is beneficial to adsorption of ammonia provides more contact time for catalyst and ammonia.

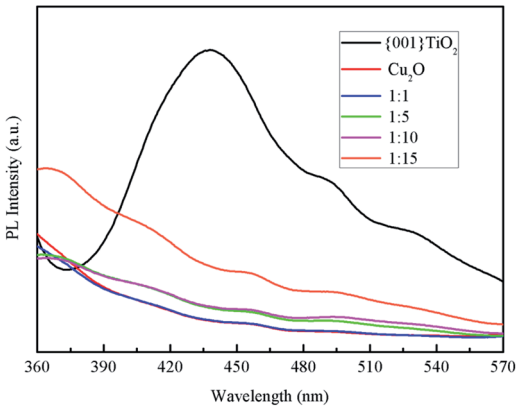


Fig. 8 PL spectrum of the samples.

### 3.6 PL analysis

Fluorescence spectroscopy is a characterization of the photo-generated electron–hole recombination of the photocatalyst, the higher the photo-generated electron–hole binding rate, the stronger the fluorescence intensity.[30] It can be seen from Fig. 8 that the electron–hole loading rate of pure {001}$TiO_2$ was higher than that of the composited catalysts, indicating that the electron–hole recombination rate of the composited catalyst was significantly reduced, the degradation efficiency of the composite catalyst in the degradation process will be significantly improved.

### 3.7 Optical performance analysis

It can be seen from Fig. 9(a) that the light absorption intensity of the composite catalysts at 350–800 nm was stronger than that of single {001}$TiO_2$, indicating that the composite catalyst had strong catalytic activity mainly in visible light range. Kubelka–Munk method was used to calculate the band gap width, as shown in eqn (1)–(3):[32]

$$A = -\lg R \quad (1)$$

$$F_{(R)} = (1 - R)^2/2R \quad (2)$$

$$(hvF) \sim (hv - E_g)^2 \quad (3)$$

where: $A$ is absorbance; $R$ is the reflection; $F_{(R)}$ is a function of Kubelka–Munk; $hv$ is the photon energy; $E_g$ is the forbidden band width of catalyst. $E_g$ of the catalysts can be obtained by

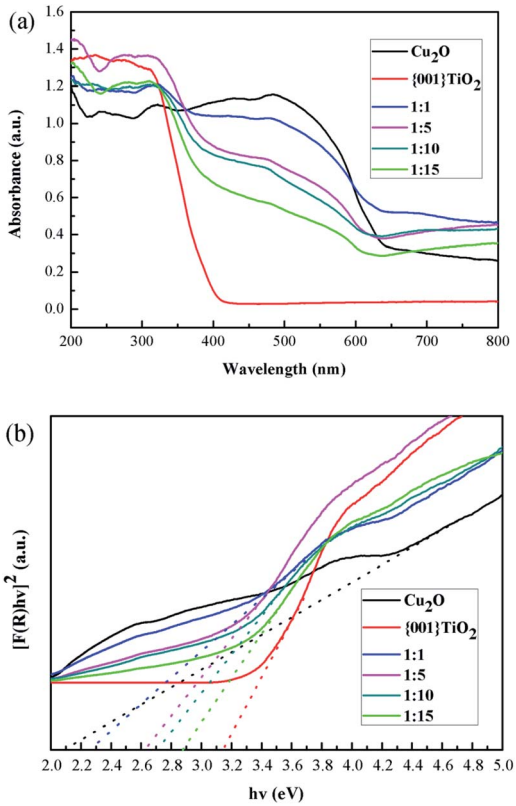


Fig. 9 Optical properties (a) UV-visible absorption spectrum of samples, (b) band gap width of the samples.

plotting the indirect relation between $(hvF)^{1/2}$ and $hv$. The energy gap of different catalysts can be calculated by linear fitting of the curve in Fig. 9(b), $E_g$ value is determined by the intercept on the $X$-axis, and the result is shown in Table 2:

The calculated results showed that the band gap width of the composite catalyst is reduced compared with that of $\{001\}TiO_2$, indicating that the composite catalyst is more easily excited and has higher catalytic activity.

### 3.8 Photocatalytic performance test

**3.8.1 Effects of different catalysts on ammonia degradation.** It can be seen from Fig. 10 that the average values of ammonia degradation rate of blank group, P25, $\{001\}TiO_2$, 1 : 1, 1 : 5, 1 : 10 and 1 : 15 were 5%, 10%, 32%, 30%, 51%, 85% and 59%, respectively, and the degradation rate of blank carrier for

Table 2 Band gap width of catalysts

| Samples | Bandgap (eV) |
|---|---|
| $Cu_2O$ | 2.12 |
| $\{001\}TiO_2$ | 3.14 |
| 1 : 1 | 2.26 |
| 1 : 5 | 2.62 |
| 1 : 10 | 2.70 |
| 1 : 15 | 2.88 |

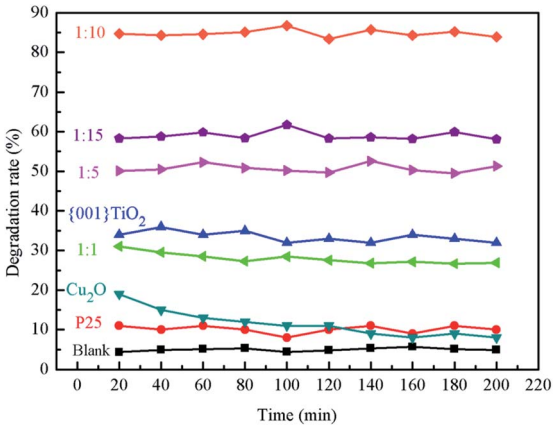


Fig. 10 The degradation of different samples on ammonia.

ammonia gas was about 5%, which indicates that the adsorption effect of carrier on ammonia was not obvious. P25, $Cu_2O$, 1 : 1 and $\{001\}TiO_2$ have low degradation rates for ammonia, because P25 and $\{001\}TiO_2$ have low utilization of sunlight. 1 : 1 was because the $Cu_2O$ content in the composite catalyst accounts for leadingly, although $Cu_2O$ itself has a strong light absorption, it is difficult to directly oxidize water to produce hydroxyl radicals, which makes it almost only adsorbent to ammonia. When the content of $\{001\}TiO_2$ in the composite catalyst gradually increased, the degradation performance of the composite catalyst for ammonia gas gradually improved, among which the degradation rate of 1 : 10 was the highest due to the maximum specific surface area.

**3.8.2 Stability test of sample.** It can be seen from Fig. 11 that the degradation rate of ammonia will decrease with the increase of material usage. The catalyst degradation rate of still maintained more than 75% in the first three times of repeated use, which decreased significantly at the fourth and fifth times. This is because there was a loss of catalyst in each repeated experiment, which ultimately led to a reduction in the degradation efficiency. In addition, the degradation rate at 200 min is lower than that at the beginning of each repeated degradation, which may be caused by photo-corrosion.

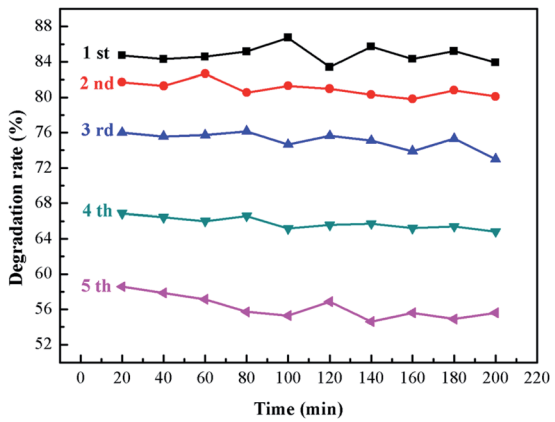


Fig. 11 The stability of 1 : 10.

**3.8.3 Reaction mechanism.** The literature showed that the peak near 1630 $cm^{-1}$ was attributable to water molecules absorbed on the catalyst surface, the absorption peak near 3423 $cm^{-1}$ was due to hydroxyl radicals formed by the intermolecular association of hydroxyl groups, and the peak near 1236 $cm^{-1}$ was $NH_3$ attached to the Lewis acid site;[33] the peak near 1414 $cm^{-1}$ was $NO_3^-$;[34] the peak in the range of 3670–3675 $cm^{-1}$ was free hydroxyl radical.[35]

It can be seen from Fig. 12 that the absorption peak at 1236 $cm^{-1}$ gradually disappeared and the ammonia molecules connected to the Lewis acid site on the catalyst surface also gradually disappeared with the extension of the reaction time. The ammonia gas in the reaction tube was not detected after the reaction for 30 min.

There had no peak at 1414 $cm^{-1}$ and 3423 $cm^{-1}$ at 0 min, but peaks were detected at 10, 20, and 30 minutes of reaction, which indicated that the associated hydroxyl radicals on the catalyst surface will be consumed and $NO_3^-$ was generated along with the reaction.

There had a peak at 1630 $cm^{-1}$ at 0 min, but no peak was detected at 10, 20, and 30 min, which indicated that the adsorption of water on the surface of the catalyst will also participate in the reaction. This may be due to the strong absorption of light energy when the carriers are separated. Oxidative holes can oxidize water molecules to hydroxyl radicals. There had no peaks in the range of 3670–3675 $cm^{-1}$ at 0 min, but had peaks at 10 and 20 min of reaction, which indicates that free hydroxyl radicals were generated during the reaction process, and at 30 min there was no peak that because the reaction has been completed. H. M. Wu *et al.* pointed out that the product distribution during the photocatalytic oxidation of $NH_3$, $N_2$ was found to be the main gaseous product;[36] $N_2O$, $NO_2^-$ and $NO_3^-$ were registered as the major by-products. In our experiment, we found $NO_3^-$ generation, because $N_2O$ and $N_2$ are gases and cannot be detected, and $NO_2^-$ will soon be oxidized and cannot be detected.

In general, the adsorption of water on the surface and the associated hydroxyl radicals participated in the reaction of degrading ammonia during the entire reaction process, and finally free hydroxyl radicals and $NO_3^-$ were formed.

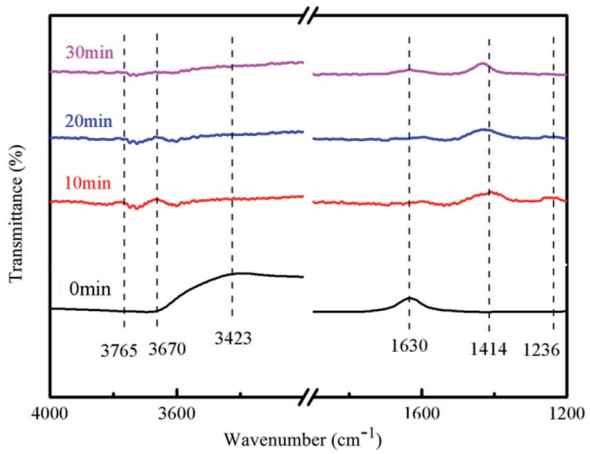


Fig. 12 FT-IR spectra at different reaction time points.

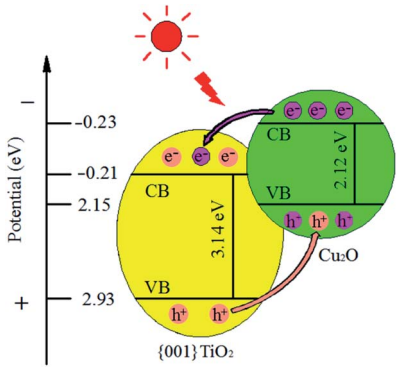


Fig. 13 Schematic mechanism of the charge transfer mechanism in $Cu_2O$/{001}$TiO_2$ system on irradiation.

**3.8.4 Mechanism of the composite.** The conduction band position of semiconductor can be calculated by empirical formula:[37] $E_c = X - E_o - E_g/2$, $E_v = E_c + E_g$. Among them $E_c$ stands for the conduction band energy of the semiconductor samples, $X$ stands for the geometric average of the absolute electronegativity of atoms in semiconductor samples, the $X$ values of $Cu_2O$ and {001}$TiO_2$ are about 5.33 and 5.86 eV, respectively. $E_o$ stands for a constant relative to the standard hydrogen electrode (4.5 eV), $E_g$ stands for the band gap width of semiconductor samples, and $E_v$ on behalf of the valence band energy of semiconductor samples. After calculation, The $E_g$ values of $Cu_2O$ and {001}$TiO_2$ were 2.12 and 3.14 eV, the $E_c$ values of $Cu_2O$ and {001}$TiO_2$ were −0.23 and −0.21 eV, and the $E_v$ values were 1.89 and 2.93 eV, respectively, as shown in Fig. 13. When exposed to light, the electrons of single $Cu_2O$ and {001}$TiO_2$ absorb energy and migrate from VB to CB, forming holes. However, the lifetime of electrons and holes generated by light is very short, and most of the charges will be recombined quickly. When the composite catalyst is synthesized, electrons excited by CB in $Cu_2O$ will be transferred to {001}$TiO_2$. At the same time, the holes generated from VB in {001}$TiO_2$ are transferred to $Cu_2O$ holes, which reduces the electron–hole pairs recombination and improves the catalytic efficiency.[37]

## 4. Conclusion

In this chapter, a chemical-impregnation method was used to prepare composite catalysts with different ratios of $Cu_2O$/{001}$TiO_2$ to degrade ammonia. The results showed that when the composite ratio was 1 : 10, the catalyst has the largest specific surface area and the highest ammonia removal efficiency. During the whole reaction process, the surface adsorbed water and associated hydroxyl radicals participated in the reaction of degrading ammonia gas, and finally formed free hydroxyl radicals and $NO_3^-$.

## Conflicts of interest

There are no conflicts to declare.

## Acknowledgements

This work was financially supported by Chongqing Technology Innovation and Application Demonstration Special Social and People's Livelihood Key Research and Development Project (cstc2018jscx-mszdX0045), Special Project for Performance Guidance of Scientific Research Institution in Chongqing (cstc2020jxjl20006), Chongqing Rongchang Agriculture and Animal Husbandry High-Tech Industry Research and Development Project (19248), the Earmarked Fund for Modern Agro-industry Technology Research System (CARS-35), and Scientific Observation and Experiment Station of Livestock Equipment Engineering in Southwest, Ministry of Agriculture. In addition, I would like to thank my wife Yi Hu for her support to my work.

## References

1 J. Lelievel, J. S. Evans, M. Fnais, *et al.*, *Nature*, 2015, **525**, 367–371.
2 S. E. Bauer, K. Tsigaridis and R. Miller, *Geophys. Res. Lett.*, 2016, **43**, 5394–5400.
3 M. V. Damme, L. Clarisse, S. Whitburn, *et al.*, *Nature*, 2018, **564**, 99–103.
4 Y. S. Wang, J. k. Zhang and L. L. Wang, *Adv. Earth Sci.*, 2013, **28**(03), 353–363.
5 G. Schauberger, M. Piringer, C. Mikovits, *et al.*, *Biosyst. Eng.*, 2018, **175**, 106–114.
6 Z. Y. Xu, M. G. Liu, M. S. Zhang, *et al.*, *Atmos. Chem. Phys.*, 2019, **19**, 5605–5613.
7 Y. Y. Wu, B. G. Gu, J. W. Erisman, *et al.*, *Environ. Pollut.*, 2016, **218**, 86–94.
8 S. H. Pu, D. B. Long, Z. H. Liu, *et al.*, *Catalysts*, 2018, **8**, 189.
9 R. G. He, H. J. Liu, H. M. Liu, *et al.*, *J. Mater. Sci. Technol.*, 2020, **17**, 145–151.
10 A. H. Kianfar and M. A. Arayesh, *J. Environ. Chem. Eng.*, 2020, **8**(1), 103640.
11 W. Y. Diao, H. Y. Cai, L. Wang, *et al.*, *ChemCatChem*, 2020, **12**(21), 5420–5429.
12 A. V. Hernández, R. A. E. Muñoz, F. J. M. Flores, *et al.*, *Mater. Sci. Semicond. Process.*, 2020, **114**, 105082.
13 M. Lettieri, D. Colangiuli, M. Masieri, *et al.*, *Build. Environ.*, 2019, **147**, 506–516.
14 G. Moupiya, M. Moumita, M. Samir, *et al.*, *J. Mol. Struct.*, 2020, **1211**, 128076.
15 H. Atout, D. Chebli, D. Tichit, *et al.*, *Mater. Res. Bull.*, 2017, **95**, 578–587.
16 N. R. Khalid, A. Majid, M. Bilal Tahir, *et al.*, *Ceram. Int.*, 2017, **43**, 14552–14571.
17 A. Busiakiewicz, A. Kisielewska, I. Piwonski, *et al.*, *Vacuum*, 2019, **163**, 248–254.
18 Y. L. Sui, L. Wu, S. K. Zhong, *et al.*, *Appl. Surf. Sci.*, 2019, **480**, 810–816.
19 H. Park and W. Choi, *J. Phys. Chem. B*, 2004, **108**(13), 4086–4093.
20 H. G. Yang, C. H. Sun, S. Z. Qiao, *et al.*, *Nature*, 2008, **453**(7195), 638–641.
21 B. Wang, L. Deng, L. Sun, *et al.*, *Sens. Actuators, B*, 2018, **276**, 57–64.
22 Q. Yang, M. Long, L. Tan, *et al.*, *ACS Appl. Mater. Interfaces*, 2015, **7**, 12719–12730.
23 X. M. Liu, L. M. Cao, W. Sun, *et al.*, *Res. Chem. Intermed.*, 2016, **42**, 6289–6300.
24 J. D. Peng, H. H. Lin, C. T. Lee, *et al.*, *RSC Adv.*, 2016, **6**, 14178–14191.
25 X. Wen, M. Long and A. d. Tang, *J. Electroanal. Chem.*, 2017, **785**, 33–39.
26 K. Lv, Q. J. Xiang and J. G. Yu, *Appl. Catal., B*, 2011, **104**, 275–281.
27 C. A. Damato, R. Giovannetti, M. Zannotti, *et al.*, *Appl. Surf. Sci.*, 2018, **441**, 575–587.
28 Z. Y. Zhang, K. C. Liu, Y. N. Bao, *et al.*, *Appl. Catal., B*, 2017, **203**, 599–606.
29 L. Ying, Z. G. Xu, Y. C. Chu, *et al.*, *Appl. Catal., B*, 2018, **224**, 239–248.
30 C. L. Yu, K. Yang, Q. Shu, *et al.*, *Chin. J. Catal.*, 2011, **32**, 555–565.
31 C. T. Hou, B. Hu and J. M. Zhu, *Catalysts*, 2018, **8**, 575.
32 B. X. Li and Y. F. Wang, *Superlattices Microstruct.*, 2010, **47**, 615–623.
33 L. Qiu, D. D. Pang, C. L. Zhang, *et al.*, *Appl. Surf. Sci.*, 2015, **357**, 189–196.
34 M. A. Debeila, N. J. Coville, M. S. Scurrell, *et al.*, *Appl. Catal., A*, 2005, **291**(1–2), 98–115.
35 S. Yamazoe, T. Okumura, Y. Hitomi, *et al.*, *J. Phys. Chem. C*, 2007, **111**(29), 11077–11085.
36 H. M. Wu, J. Z. Ma, Y. B. Li, *et al.*, *Appl. Catal., B*, 2014, (152–153), 82–87.
37 L. Yang, Z. G. Miao, K. R. Zhu, *et al.*, *Appl. Surf. Sci.*, 2017, **391**, 353–359.